Effect of boron doping on the wear behavior of the growth and nucleation surfaces of micro- and nanocrystalline diamond films

Buijnsters, J.G.; Tsigkourakos, Menelaos; Hantschel, T.; Gomes, F.O.V.; Nuytten, T.; Favia, P.; Bender, H; Arstila, K.; Celis, JP; Vandervorst, W

DOI
10.1021/acsami.6b08083

Publication date
2016

Document Version
Accepted author manuscript

Published in
ACS Applied Materials and Interfaces

ACS APPLIED MATERIALS & INTERFACES

Research Article

www.acsami.org

Effect of Boron Doping on the Wear Behavior of the Growth and Nucleation Surfaces of Micro- and Nanocrystalline Diamond Films

Josephus G. Buijnsters,*[,†,⊥] Menelaos Tsigkourakos,[†,‡,§] Thomas Hantschel,[‡] Francis O. V. Gomes,[‡,§] Thomas Nuytten,[‡] Paola Favia,[‡] Hugo Bender,[‡] Kai Arstila,[‡,∥] Jean-Pierre Celis,[⊥] and Wilfried Vandervorst[‡,§]

[†]Department of Precision and Microsystems Engineering, Research Group of Micro and Nano Engineering, Delft University of Technology, Mekelweg 2, 2628 CD Delft, The Netherlands

[‡]Imec, Kapeldreef 75, B-3001 Leuven, Belgium

[§]IKS-Department of Physics, KU Leuven, Celestijnenlaan 200D, B-3001 Leuven, Belgium

[∥]Department of Physics, University of Jyväskylä, P.O. Box 35, FI-40014 Jyväskylä, Finland

[⊥]Department of Materials Engineering, KU Leuven, Kasteelpark Arenberg 44, B-3001 Leuven, Belgium

Supporting Information

ABSTRACT: B-doped diamond has become the ultimate material for applications in the field of microelectromechanical systems (MEMS), which require both highly wear resistant and electrically conductive diamond films and microstructures. Despite the extensive research of the tribological properties of undoped diamond, to date there is very limited knowledge of the wear properties of highly B-doped diamond. Therefore, in this work a comprehensive investigation of the wear behavior of highly B-doped diamond is presented. Reciprocating sliding tests are performed on micro- and nanocrystalline diamond (MCD, NCD) films with varying B-doping levels and thicknesses. We demonstrate a linear dependency of the wear rate of the different diamond films with the B-doping level. Specifically, the wear rate increases by a factor of 3 between NCD films with 0.6 and 2.8 at. % B-doping levels. This increase in the wear rate can be linked to a 50% decrease in both hardness and elastic modulus of the highly B-doped NCD films, as determined by nanoindentation measurements. Moreover, we show that fine-grained diamond films are more prone to wear. Particularly, NCD films with a 3× smaller grain size but similar B-doping levels exhibit a double wear rate, indicating the crucial role of the grain size on the diamond film wear behavior. On the other hand, MCD films are the most wear-resistant films due to their larger grains and lower B-doping levels. We propose a graphical scheme of the wear behavior which involves planarization and mechanochemically driven amorphization of the surface to describe the wear mechanism of B-doped diamond films. Finally, the wear behavior of the nucleation surface of NCD films is investigated for the first time. In particular, the nucleation surface is shown to be susceptible to higher wear compared to the growth surface due to its higher grain boundary line density.

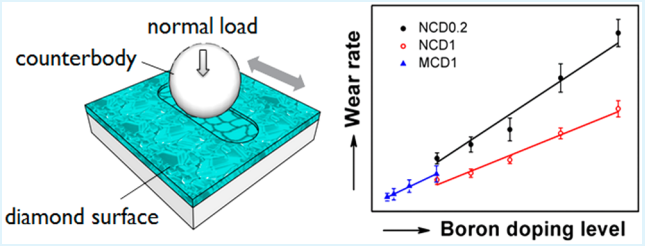

KEYWORDS: *diamond films, boron doping, wear, nucleation surface, reciprocating sliding, planarization*

1. INTRODUCTION

Diamond is an exceptional engineering material with outstanding properties such as extreme hardness (Vickers hardness ∼100 GPa), high elastic modulus (∼1200 GPa), high thermal conductivity at room temperature (20 $W \cdot cm^{-1} \cdot K^{-1}$), and chemical inertness.[1,2] The rapid development of chemical vapor deposition (CVD) techniques for the synthesis of diamond thin films in the 1990s resulted in various engineering applications such as cutting tools,[3,4] wear-resistant coatings,[5,6] and diamond-coated pump seals.[7] Moreover, CVD diamond films can be made electrically conductive by the addition of boron dopant atoms within the diamond matrix. The electrical properties of B-doped diamond can vary from insulating over semiconducting to nearly metallic according to the B-doping level, whereby an abrupt semiconductor−metal transition occurs at a boron concentration of about 10^{20} cm^{-3} (i.e., 0.06 at. %).[8] Above this doping level, the B-doped diamond films exhibit low resistivity values, in the range of 5×10^{-3} Ω cm.[9] This allows for a wide range of different applications such as in microelectromechanical systems (MEMS) for high-frequency resonators[10,11] and electrical probes for atomic force microscopy (AFM), in particular applied in scanning spreading resistance microscopy (SSRM)[12,13] and scanning electrochemical microscopy.[14] Furthermore, B-doped diamond films are used as electrochemical[15−17] and corrosion-resistant electrodes for water purification[18] and electro-oxidation

Received: July 3, 2016
Accepted: September 5, 2016

DOI: 10.1021/acsami.6b08083
ACS Appl. Mater. Interfaces XXXX, XXX, XXX−XXX

purposes,[19,20] electrochemical capacitors for energy storage,[21] as well as biocompatible electrodes for implants.[22,23]

Diamond polishing has been investigated thoroughly for about 100 years because of its evident importance in jewelry.[24] Many works revealed the polishing anisotropy of single-crystal diamond that correlates with "soft" and "hard" crystallographic surfaces and polishing directions exhibiting high and low wear rates, respectively.[25−27] Recently, Pastewska et al.[28] used classic molecular dynamics to elucidate the microscopic processes underlying diamond polishing. They showed that polished diamond undergoes an sp^3 to sp^2 order−disorder transition by mechanochemical amorphization. The tribological behavior of undoped CVD polycrystalline diamond films has been widely studied as well and has been shown to be dependent on various parameters such as the grain size, hardness, elastic modulus, and counterbody material.[29−34] To date, however, there is a very limited understanding of the wear performance of B-doped diamond films. Previous studies did not apply different B-doping levels and thus do not provide any conclusive statements on the effects of B-content on the wear response of B-doped diamond films. A research study by Liang et al.[35] focused on the tribological properties of the growth surface of nanocrystalline diamond (NCD) films doped with nitrogen and/or boron atoms. It was found that the wear rate of B-doped and B/N-codoped NCD films is significantly higher (about 1 order of magnitude) than that of N-doped NCD films, which was attributed to the boron incorporation. On the other hand, Wang et al.[36] reported an improvement of the wear resistance and adhesive strength of diamond films to WC-Co inserts by B-doping in cutting applications. Apparently, a clear understanding of the role of boron dopants in the wear behavior of the diamond films is still missing.

Many diamond applications utilize the nucleation surface of the electrically conductive (B-doped) diamond film as the active layer.[37] Therefore, there is a strong demand for a highly wear-resistant nucleation side of the B-doped diamond films, especially for SSRM tips[12] and MEMS[10] applications. As the growth surface of B-doped diamond films (rough, last grown layer) is significantly different from the nucleation surface (smooth, first grown layer), it is necessary to investigate the wear of highly B-doped films also directly on the nucleation surface and compare it to that on the growth surface. Compared to the growth surface, where sliding wear tests can be directly performed, wear studies on the nucleation surface require the careful and precise removal of the substrate material without damaging the nucleation surface. The diamond membrane must then be mounted in a suitable manner on a supporting substrate for testing. Such an approach has only been applied successfully so far to study the elemental and electrical properties of the nucleation surface,[38,39] as well as the interfacial adhesion and friction between commercial diamond-coated AFM tips and the growth/nucleation surfaces of undoped ultrananocrystalline diamond (UNCD) films.[40,41] However, experimental data on the tribological response of the nucleation surface in comparison to the growth surface of B-doped diamond films are not yet available in the literature.

Therefore, this paper presents the wear performance of the growth surface of diamond films of various B-doping levels and compares it to the nucleation surface. To identify the tribological behavior on a macroscopic scale, sliding tests were performed in ambient air in which the two contacting solids are subjected to a small amplitude oscillation.[29,31] This is done for both B-doped NCD and microcrystalline diamond (MCD) films, as the latter have a larger average grain size and hence fewer grain boundaries.[42] Based on the experimental observations, a graphical scheme is proposed that includes an atomistic view of the wear mechanism of B-doped diamond surfaces. The main novelty of this work is the systematic variation of B-content in a variety of diamond film types and thus contributes to a better understanding of the tribological properties and specifically the wear behavior of electrically conductive diamond films according to their B-doping level and grain size.

2. EXPERIMENTAL SECTION

2.1. Diamond Film Preparation. Four different types of diamond films (3× NCD, 1× MCD) with two film thicknesses (0.2 and 1 μm) and varying B-doping levels are studied. Table 1 provides the specific details of the different diamond films.

Prior to CVD diamond growth, four Si(100) wafer substrates (⌀ 200 mm) are spin-seeded with 5 nm sized diamond nanoparticles (NanoAmando aqueous colloid, NanoCarbon Research Institute), as described elsewhere.[43] A seeding density of about 5×10^{10} cm^{-2} is established. The seeded wafers are then transferred to a hot-filament CVD (HFCVD) reactor (sp^3 Diamond Technologies, model 655), and the different diamond films are grown using a three-gas chemistry of hydrogen (H_2), methane (CH_4), and trimethyl boron (TMB). The CH_4/H_2 gas ratio is set at 2.4 and 1.5% and the pressure at 8 and 33 mbar resulting in NCD and MCD films, respectively. The substrate temperature is about 850 °C during growth. The TMB flow is adjusted in different depositions to attain the full range of resistivity values from high (>20 Ω cm, lowly doped due to background doping from boron-contaminated reactor chamber walls) to very low, nearly metallic-like, values ($\sim 5 \times 10^{-3}$ Ω cm).[44] The B-doping level varies from 0.6 to 2.8 at. % in the NCD films and from 0.03 to 0.6 at. % in the MCD films, as measured by secondary ion mass spectroscopy (SIMS) (Atomika 4500 quadrupole instrument, Cameca) with a Cs^+ primary beam (5 keV impact energy at 45° to sample normal). The exposure of the nucleation surface of the NCD film (i.e., "NCD1-nucl" sample) requires additional sample preparation as illustrated in Figures 1b and 1c: an additional undoped NCD layer (15 μm thickness) is grown on top of the growth surface of the NCD film to provide mechanical support, and subsequently the Si substrate is removed by wet etching with 30% (w/v) KOH at 85 °C. After rinsing in H_2O and drying with N_2, the diamond membrane is then carefully turned around and glued (Loctite 406) onto a silicon supporting substrate with the nucleation surface facing upward. Elastic recoil detection (ERD) measurements of the nucleation surface showed there is no significant Si incorporation into the diamond matrix compared to boron.[39]

2.2. Reciprocating Sliding Tests. Sliding tests at applied normal load in the Newton range are performed at the macroscale under unlubricated reciprocating sliding in a ball-on-flat configuration[45] on the growth (Figure 1a) and nucleation surface (Figure 1c). The sliding tool allows for real-time monitoring of the linear contact displacement, the applied normal force, and the tangential force as a function of time over the interval of one cycle and over the total test duration. The gross-slip wear tests are performed for different total number of cycles

Table 1. Comparison of the Different Diamond Samples Used in This Study

sample	NCD1-nucl	NCD0.2	NCD1	MCD1
type of film	NCD	NCD	NCD	MCD
measured surface	nucleation	growth	growth	growth
film thickness (μm)	1.0	0.2	1.0	1.0
rms roughness (nm)	0.6	14	24	68
boron doping level (at. %)	2.8	0.6, 1.0, 1.5, 2.1, 2.8	0.6, 1.0, 1.5, 2.1, 2.8	0.03, 0.1, 0.3, 0.6

DOI: 10.1021/acsami.6b08083
ACS Appl. Mater. Interfaces XXXX, XXX, XXX−XXX

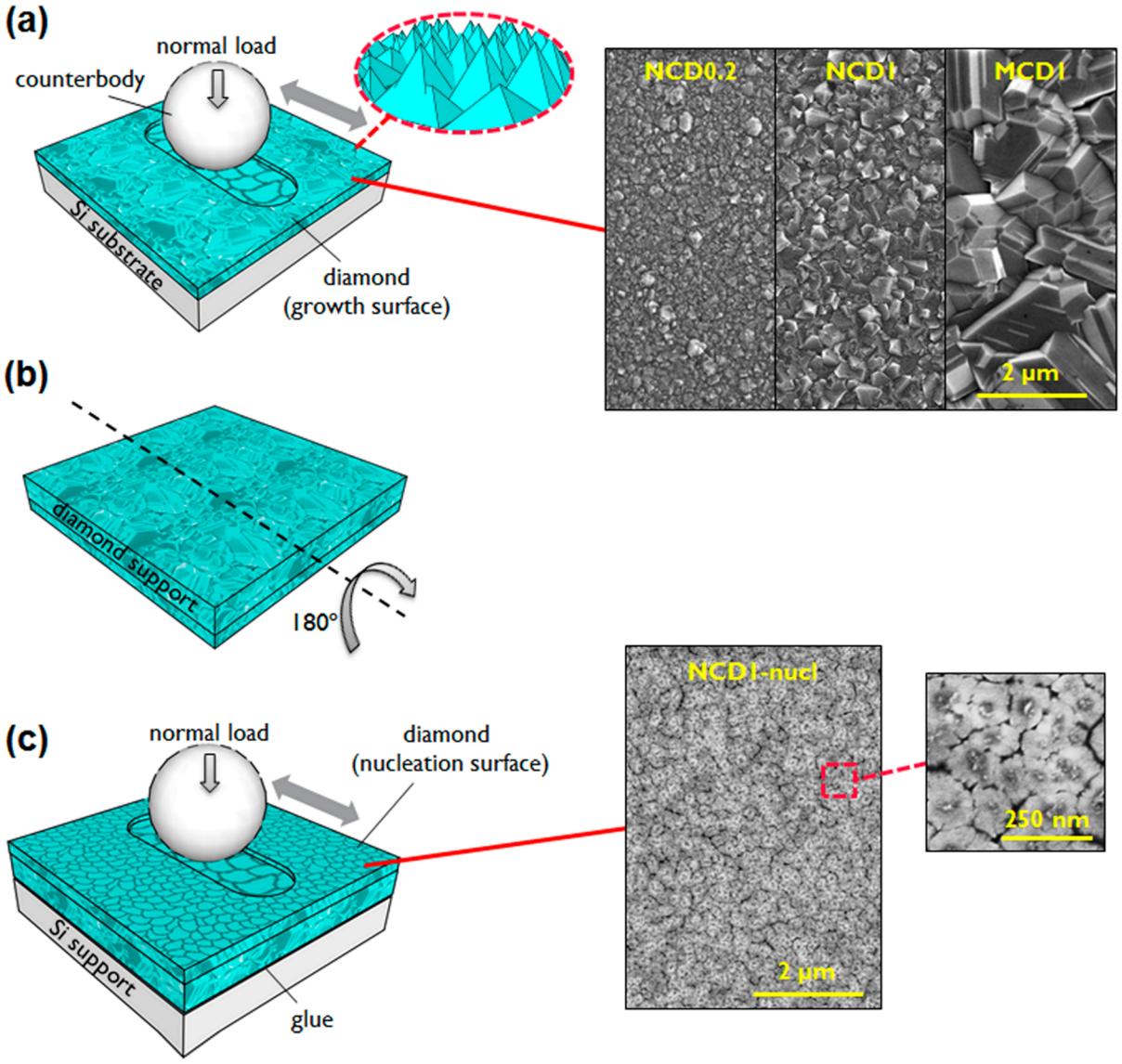

Figure 1. Schematic of the experimental approach showing the ball-on-flat reciprocating sliding tests being performed on the growth and nucleation surfaces of the diamond films, respectively. (a) Tests performed on the growth surface. (b) Freestanding diamond membrane (16 μm thickness) is produced by growth of an additional undoped NCD layer (15 μm thickness) on top of the NCD film, followed by removal of Si substrate. (c) The membrane is turned around and glued on a silicon supporting substrate with the nucleation surface facing upward, whereby sliding tests are performed. SEM images of the growth surfaces of the NCD0.2, NCD1, and MCD1 films (top) as well as the nucleation surface, NCD1-nucl, (bottom) are added.

(250, 1000, 2000, 3000, and 10000) at 5 Hz frequency. The sliding displacement amplitude is 200 μm, and the applied normal load is 2 N. The atmospheric conditions during the sliding tests are a relative humidity of 55% and a temperature of 23 °C. Two different counterbody ball (⌀ 10 mm) materials are used: polished alumina (Al_2O_3) with a root-mean-square (rms) surface roughness of 22 nm (Ceratec Technical Ceramics BV) and diamond-coated hard metal (Diamond Product Solutions), which is used for the sliding tests on the nucleation surface of the diamond film. In the case of the diamond-coated hard metal balls (or diamond-coated balls for simplicity), three different diamond coatings are used: polished NCD (PN), rough NCD (RN), and rough MCD (RM) with rms surface roughness values of 4, 380, and 210 nm, respectively. The applied normal force of 2 N corresponds to maximum Hertzian contact pressures in the range of about 0.9 and 1.4 GPa for the alumina and diamond counterbodies, respectively.

2.3. Nanoindentation. Nanoindentation measurements (CSM, TTX-NHT) are performed by applying maximum normal loads of 10 mN using a Berkovich diamond indenter tip. The normal load is reduced to relaxation with a dwell time of 5 s upon reaching the preset value. Both loading and unloading times are 30 s. For each cycle of loading and unloading, a force versus displacement curve is obtained from which the hardness and elastic modulus are deduced from the unloading curve, using the Oliver–Pharr method.[46] As a rule of thumb, the maximum penetration depth is kept below ~10% of the total film thickness to avoid the influence of the underlying substrate on the measurement results.

2.4. Characterization of the As-Deposited and Worn Diamond Films. The maximum wear depth at the center of the wear tracks after sliding is studied using a white-light interferometry (WLI) tool (Bruker, Wyko NT3300). The wear volume obtained through WLI was used to calculate the wear rate coefficient (k) by using Archard's law: $k = V/F_nS$ where V is the wear volume, F_n the applied normal load, and S the total sliding distance.[47] The rms surface roughness of the wear tracks formed on the B-doped diamond films is measured using an AFM instrument (Bruker, Dimension 3000) in ambient atmosphere. Scanning electron microscopy (SEM) imaging (FEI, XL30) is performed at 5 kV accelerating voltage to investigate

DOI: 10.1021/acsami.6b08083
ACS Appl. Mater. Interfaces XXXX, XXX, XXX−XXX

the surface morphology of the B-doped diamond films before and after testing. Energy-dispersive X-ray spectroscopy (EDX) measurements are done with a Si(Li) detector (EDAX) to analyze the debris from both the counterbody ball and the diamond films. Transmission electron microscopy (TEM) analysis is done on focused ion beam prepared cross-sectional specimens in TEM and scanning TEM (STEM) mode (FEI, Tecnai F30). Raman spectroscopy measurements (Horiba, LabRAM HR) are performed using a laser wavelength of 532 nm and a power density of 200 $\mu W/\mu m^2$.

3. RESULTS AND DISCUSSION

3.1. Morphological and Crystalline Structure Analysis of the As-Deposited Diamond Films. The SEM images in Figure 1 illustrate the surface morphology of the as-deposited growth surfaces of the different NCD and MCD films, as well as the nucleation surface of the NCD film (NCD1-nucl). The MCD1 film shows a highly faceted growth surface, and its average surface grain size[44] is about 1.1 μm, resulting in a grain boundary line density (i.e., the number of grain boundaries per unit area, whereby the surface grains are considered as squares and the grain boundaries as the sides of each square-shaped grain; the grain boundary line density is directly proportional to the number of grains per unit area) of approximately 1×10^8 cm^{-2}. The surface grains (i.e., top part of the grains visible from the top surface of the diamond film) have a wedge shape of (111) crystal orientation by virtue of their columnar growth, which results in an overall higher rms surface roughness of 68 nm. The NCD1 and NCD0.2 film surfaces exhibit diamond crystallite facets smaller than 320 and 180 nm in size, respectively, resulting in grain boundary line densities of about 1×10^9 and 3×10^9 cm^{-2} as well as rms roughness values of 24 and 14 nm. The NCD1-nucl film surface is very smooth with an rms surface roughness of only 0.6 nm. The seed diamond nanoparticles of ~20−50 nm in size are attached to the nucleation surface[38] and can be distinguished from the SEM image inset in Figure 1c (white spots), together with the grain boundaries (black narrow trenches) and the bottom side of the grains (light gray regions separated by the grain boundaries). The average grain (i.e., bottom side of the grains) size is ~100 nm which leads to a grain boundary line density of 1×10^{10} cm^{-2}.

Figure 2 shows the Raman spectra obtained from the as-deposited films with the highest B-doping levels (2.8 at. % for NCD1-nucl, NCD0.2, and NCD1 and 0.6 at. % for MCD1). These Raman spectra are composed of typical signature peaks for heavily B-doped diamond films. The sp^3-related diamond peak at ~1332 cm^{-1} can be clearly distinguished only at the spectrum of the MCD1 film. This is in close agreement with an earlier study by Bernard et al.,[48] who showed that this peak disappears for B-doping levels above ~0.5 at. % for which it remains only a shoulder. At high B-doping levels, there is a high degree of Fano interactions induced by quantum mechanical interference between the transitions from a discrete state composed by the excited acceptor levels and a continuum of the valence band states.[49] Such phonon-related interactions cause the asymmetry and broadening of the diamond peak at the Raman spectrum.[50] Therefore, the diamond peak is barely visible especially for the NCD1 and NCD0.2 films. Note that the B-doping level close to the nucleation surface of the diamond film (NCD1-nucl) is expected to be slightly lower compared to the growth surface (NCD1).[38] This effect, in combination with the presence of the embedded undoped diamond seed nanoparticles at the nucleation surface, makes the Fano interference less pronounced and thus the diamond

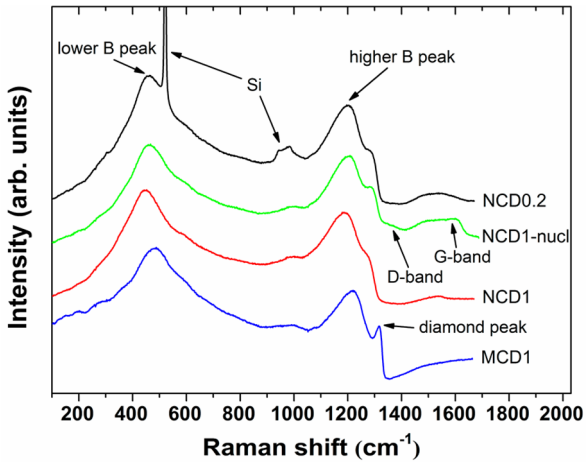

Figure 2. Raman spectra recorded on the surfaces of the as-deposited MCD1, NCD1, NCD1-nucl, and NCD0.2 films with highest boron doping level (i.e., 2.8 at. % and 0.6 at. % for the NCD and MCD films, respectively).

peak more distinguishable at the NCD1-nucl spectrum. The broad and intense boron-related peaks at ~450 and ~1200 cm^{-1}, called the lower and higher boron peak, respectively, dominate all the Raman spectra and arise from the incorporation of high levels of boron dopants into the diamond lattice. A down-shift in the lower B peak is observed with increasing boron content[48] in the order MCD1 > NCD1-nucl > NCD0.2, NCD1. Moreover, silicon-related peaks at ~520 and ~960 cm^{-1} are recorded from the NCD0.2 film only. These peaks are attributed to the underlying silicon substrate that is probed by the laser as a result of the low diamond film thickness of 200 nm.

The broad humps at ~1350 and ~1575 cm^{-1} are known as D and G peaks, respectively, and are due to the sp^2/a-C phases at the grain boundaries.[51,52] The presence of the D peak indicates the existence of aromatic sp^2 rings, whereas the G peak can arise from sp^2-C in both rings and chains. In the case of the NCD films the D and G bands become more pronounced, as is observed for the NCD1 and NCD0.2 films, due to the higher grain boundary line density. Overall, as the grain boundary line density is higher for the films that consist of smaller grains, the amount of sp^2/a-C within the diamond films is in the order NCD1-nucl > NCD0.2 > NCD1 > MCD1. Note that the Raman spectrum of NCD1-nucl is similar to that of NCD1 because the laser probes not only the nucleation interfacial layer but also deeper (between 0.2 and 1 μm) into the diamond film.

3.2. Effect of B-Doping and Grain Size on Wear Behavior. *3.2.1. Wear Rate.* Figure 3 shows the results of the sliding and nanoindentation measurements for the growth surface of the B-doped diamond films. In particular, Figure 3a demonstrates the dependence of the wear rate of each film (MCD1, NCD1, and NCD0.2) according to the different B-doping levels. All sliding measurements were performed in ambient air for a fixed number of 3000 sliding cycles using the alumina ball while applying 2 N of normal load. A clear linear dependency of the wear rate as a function of B-doping level can be observed for each type of diamond film. Our measurements specifically show that the wear rates of all films increase by a factor of 3 over the wide range of B-doping levels used in this study. This indicates that a higher amount of boron dopants incorporated into the diamond matrix makes the films more prone to wear, as will be described in more detail later on. The

DOI: 10.1021/acsami.6b08083
ACS Appl. Mater. Interfaces XXXX, XXX, XXX−XXX

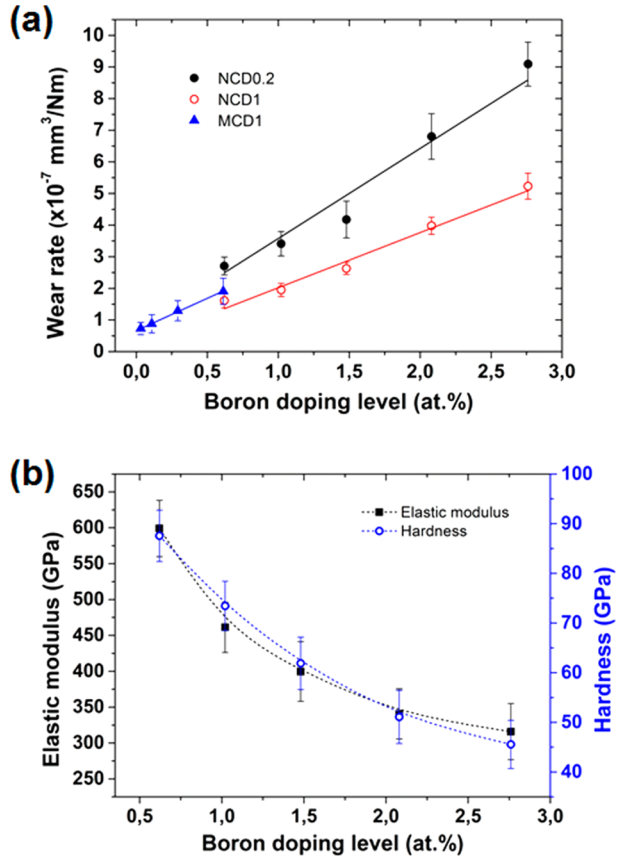

Figure 3. (a) Comparison of the wear rate vs B-doping level for the NCD1, NCD0.2, and MCD1 films after 3000 sliding cycles against an alumina ball at 2 N normal load. (b) Elastic modulus (closed squares) and hardness (open circles) vs B-doping level for the NCD1 film. Data derived from nanoindentation measurements with a maximum load of 11 mN.

wear rate between NCD0.2 and NCD1 is a factor of ~2 different at both the lowest and highest B-doping levels, with values of 1.5×10^{-7} (NCD1) and 2.7×10^{-7} mm^3/Nm (NCD0.2) at 0.6 at. % B-doping level, as well as 4.5×10^{-7} (NCD1) and 9.0×10^{-7} mm^3/Nm (NCD0.2) at 2.8 at. % B-doping level. Note that even though NCD1 and NCD0.2 films have identical B-doping levels the curve corresponding to NCD0.2 exhibits a 2× higher slope compared to the NCD1 curve. This indicates the strong effect of the higher (i.e., 3 ×) grain boundary line density on the wear of the NCD0.2 films (compared to NCD1). Hence, this difference implies that the grain boundary line density plays a crucial role in the wear behavior of the diamond films. MCD1 films exhibit the lowest wear rate among the three different series of samples due to the lower B-doping level (ranging from 0.03 to 0.6 at. %) as well as the larger grain sizes (i.e., lowest grain boundary line density of $\sim 1 \times 10^8$ cm^{-2}). However, the wear rate of the MCD1 film with the same B-doping level as the relevant NCD1 film (0.6 at. %) is similar (i.e., $\sim 1.8 \times 10^{-7}$ mm^3/Nm), even though the MCD1 film consists of larger grains. This indicates that at relatively high B concentration values of MCD films the presence of B dopants dominates their wear properties.

In conclusion, an NCD film with a low (0.6 at. %) B-doping level is 3× more wear resistant than an NCD film with a high doping level (2.8 at. %) but with the same average grain size (i.e., same grain boundary line density). MCD films are less prone to wear compared to NCD due to the larger grain sizes. Nonetheless, the wear resistance of a highly B-doped MCD deteriorates and can become comparable with that of a lowly B-doped NCD film.

3.2.2. Elastic Modulus and Hardness. Nanoindentation measurements were performed to extract the elastic modulus and hardness of NCD films with varying B-doping levels. Figure 3b illustrates the elastic modulus (E) and the hardness (H) as a function of B-doping level. As can be seen, both E and H decrease progressively from relatively high values of about 600 and 90 GPa (at 0.6 at. % B-doping level) toward lower values of 325 and 45 GPa, respectively (at 2.8 at. % B-doping level). The E and H values are significantly lower than the highest values found for single-crystal diamonds (1200 and 140 GPa, respectively)[53,54] and sintered nanocrystalline diamond.[55] They are, however, comparable to the data derived from nanoindentation measurements on rough and polished polycrystalline diamond films,[56] as well as on undoped[57] and B-doped cauliflower-type diamond films.[35] As anticipated, a maximum penetration depth (approximately 120 nm) was recorded on the film with the highest B-doping level (2.8 at. %).

The above results imply that the higher amount of incorporated boron dopants results in softer and less stiff diamond films. The negative effect of boron dopants on the wear resistance of the CVD diamond films is also anticipated from the weaker B−C bond. There is a clear difference in bond energy between B−C (322.9 kJ mol^{-1}) and C−C (357.5 kJ mol^{-1}). Furthermore, our experimental data of the wear rate (Figure 3a) as well as the mechanical properties (Figure 3b) of B-doped NCD can be explained by a theoretical calculation in the framework of the density functional method for different levels of boron doping. Li et al.[58] showed that the formation enthalpy of diamond-like B_xC_y structures roughly increases with the rise of boron concentration up to 50 at. %. Therefore, B_xC_y structures are less stable than B-free diamond. A significant drop in bulk modulus and Vickers hardness with increasing B-content was also reported.[58] Likewise, Zarechnaya et al.[59] found a (linear) decrease of the bulk modulus with the boron concentration of B-doped diamond for levels of boron doping up to 12.5 at. %. The results of both studies[58,59] are therefore well in line with our experimental data of wear rate, elastic modulus, and hardness of B-doped diamond films (Figure 3).

3.3. Wear Mechanism. *3.3.1. Surface Planarization of Diamond Film Growth Surfaces.* There is a strong formation of wear debris in and around the wear tracks formed on all the different diamond films when sliding against alumina. In particular, Figure 4a shows a SEM image of the wear track formed on the NCD1 film with the highest B-doping level (2.8 at. %) after sliding for a total of 250 cycles. As can be seen, most of the debris is located outside the scratched area at the very ends of the wear track. EDX analysis of the debris region (lighter contrast) and of the film surface at the center of the wear track (dark region) shows that the debris is mainly composed of alumina. A small amount of alumina debris is also located within the wear track. There is a strong abrasion of the alumina counter ball during the beginning of the sliding test for all samples tested. It is most pronounced when sliding takes place against the MCD1 films due to the highest rms surface roughness of the latter ones. Furthermore, all different diamond film surfaces become smoothened within the contact area. Figures 4b−d show the AFM topography images taken from the as-deposited NCD0.2, NCD1, and MCD1 film surfaces

DOI: 10.1021/acsami.6b08083
ACS Appl. Mater. Interfaces XXXX, XXX, XXX−XXX

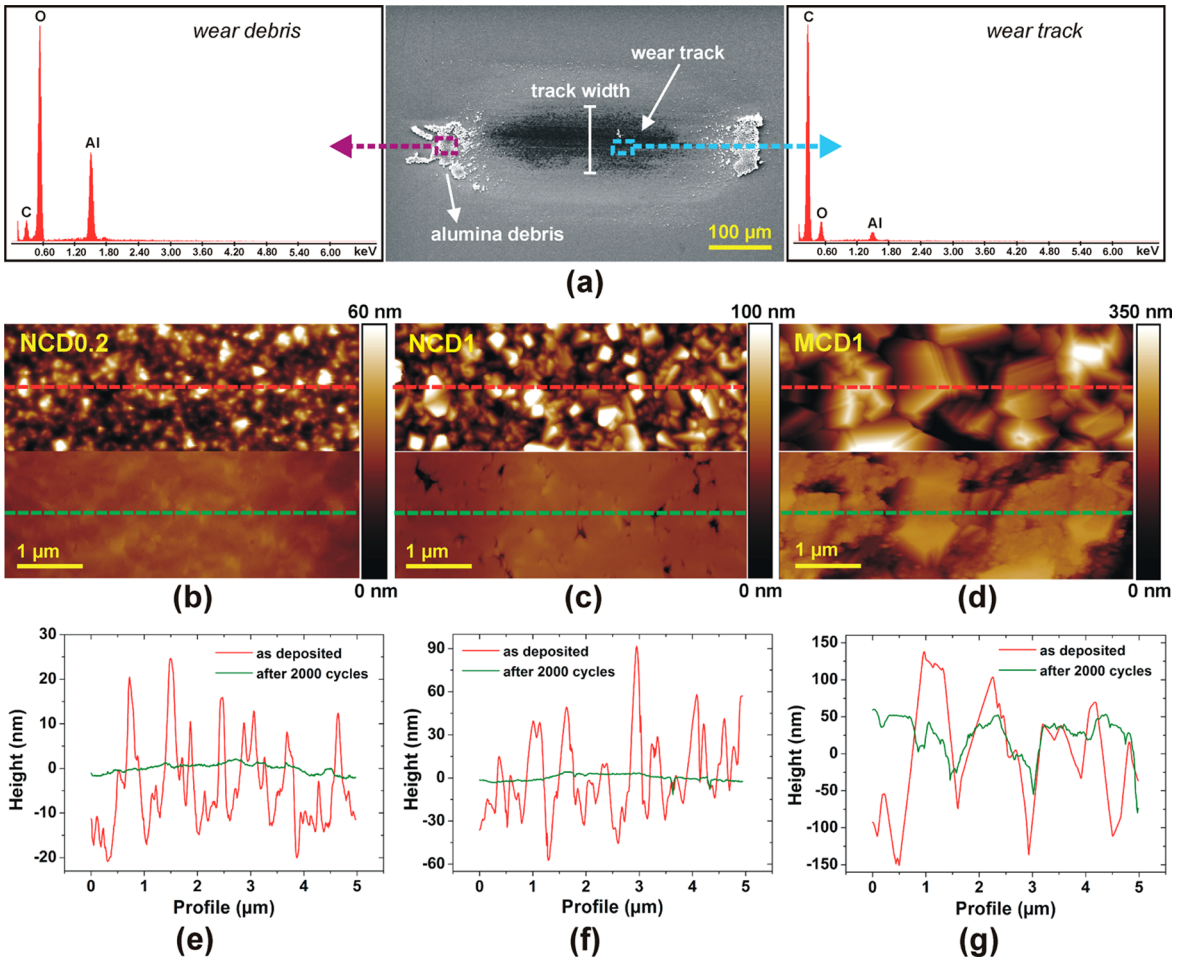

Figure 4. (a) SEM image of the wear track formed on the NCD1 (2.8 at. %) film after sliding for 250 cycles together with selective-area EDX spectra taken from the debris and the center of the wear track, respectively. (b–d) Tapping-mode AFM topography images of the as-deposited NCD1 (2.8 at. %), NCD0.2 (2.8 at. %), and MCD1 (0.6 at. %) film surfaces (upper images) and taken from the center of the wear tracks formed on these films after sliding for 2000 cycles (lower images). (e–g) Surface line-scan profiles measured on the as-deposited and worn film surfaces along the dashed red and green lines, respectively, indicated in b–d. Note the different absolute height scales among the three different graphs.

with highest B-doping levels (upper images) and those taken from the center of the wear tracks after sliding for 2000 cycles (lower images). The typical polycrystalline surface morphologies with randomly oriented, protruding diamond grains transform into highly flattened, worn surface topographies. The smoothest surface area (rms roughness ~1 nm) is obtained on the initially least rough NCD0.2 film (Figure 4b). Here, the grain boundaries cannot be distinguished well anymore as the worn surface has become very uniform in height. The initially rougher NCD1 film (Figure 4c) is smoothened to a similar extent (rms roughness ~2.5 nm), but after 2000 cycles a number of voids resulting from triple junctions of grain boundaries can still be observed. The in-time surface planarization of the NCD1 film is demonstrated in more detail in Figure S1 (AFM maps of the wear track for increasing number of cycles) and Figure S2 (rms roughness of wear track on the NCD0.2, NCD1, and MCD1 films for increasing number of cycles) of the Supporting Information. On the other hand, sliding against the rougher MCD1 films results in a surface smoothening where the larger diamond crystals are only partially flattened (Figure 4d). Note that debris is detected in-between the worn diamond grains, as will be further confirmed by the TEM analysis (see Figure 5e). Surface line-scan profiles measured on the as-deposited and worn film surfaces are displayed in Figures 4e–g. These plots highlight the drastic reduction of the surface roughness of the three different film types. The elimination of high roughness spikes on the two NCD films is evident, and also the flattening of the MCD1 film surface is clear. In the latter case, the transformation from a film surface with positive skewness (protruding micron-sized diamond grains) toward a flattened worn surface with a highly negative surface skewness (valleys are predominant) is manifest. Importantly, no abrupt failure of any of the different diamond films (i.e., adhesive loss) could be detected in our study.

Figure 5 shows dark-field STEM and TEM cross-section images of both NCD1 and MCD1 films with the highest B-doping levels (2.8 and 0.6 at. %, respectively) after 1000, 3000, and 10000 sliding cycles. The columnar growth of the NCD film can be noticed in Figures 5a–c, whereby the evolving grains competed with each other while forming a closed diamond film. As the growth progressed, less (and larger) grains per unit area eventually reached the top surface, leading to a lower grain boundary line density at the growth surface. This explains the 3× higher grain boundary line density of NCD0.2 compared to NCD1 film, as presented before. Furthermore, the surface planarization of the NCD1 film growth surface is visible as the number of sliding cycles

DOI: 10.1021/acsami.6b08083
ACS Appl. Mater. Interfaces XXXX, XXX, XXX–XXX

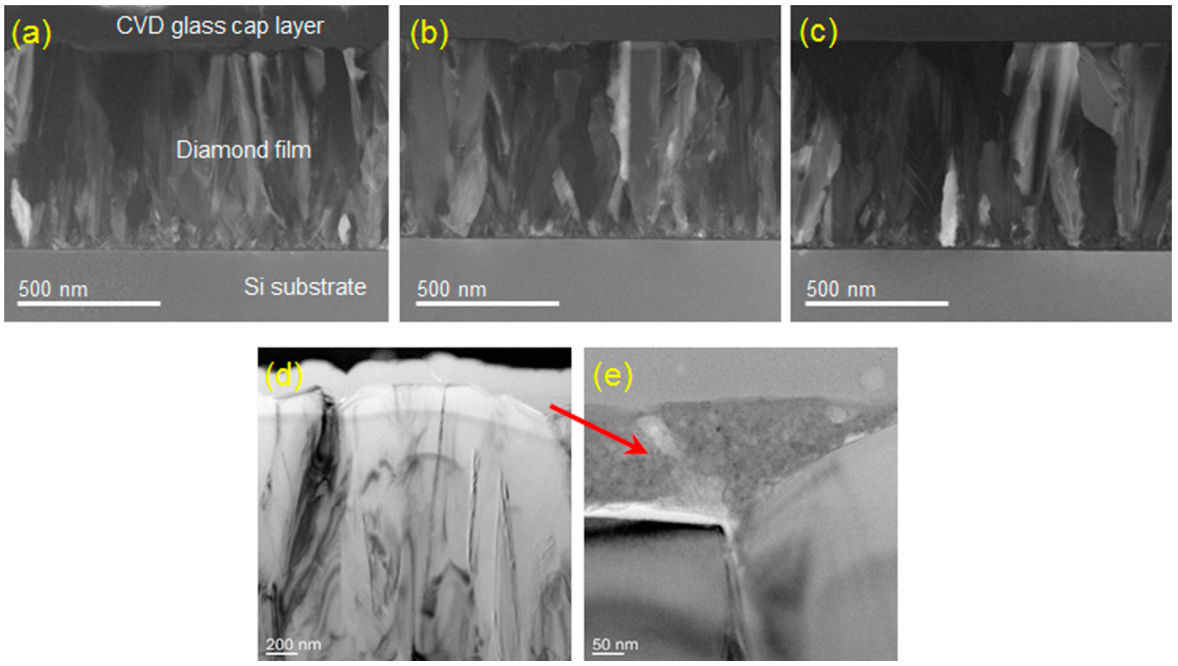

Figure 5. (a–c) Dark-field STEM cross-section image of the wear track formed on the NCD1 (2.8 at. % B) films after 1000, 3000, and 10 000 sliding cycles against alumina ball, respectively. (d) TEM cross-section of the wear track formed on the MCD1 (0.6 at. % B) film after 10 000 cycles against alumina ball. (e) Zoom-in image of the trapped debris.

increases (see Figures 5a–c). Figure 5d shows a TEM cross-section image of the MCD1 sample after 10 000 cycles. The growth surface is seemingly still rough, even after such a prolonged sliding test. However, the top surface of the protruding grains is flattened. A zoom-in image (Figure 5e) of a cavity (indicated by the arrow in Figure 5d) clearly illustrates the trapped debris in-between two large worn diamond grains, supporting the findings of the AFM analysis for the MCD1 film (see Figures 4d and g). Moreover, the STEM zoom-in image indicates that the trapped debris consists of amorphous/fine-grained polycrystalline material.

The detection of trapped debris in-between the larger worn diamond grains by AFM and TEM indicates a (partial) fill-up of the sliding contact. Together with the progressive planarization of the sample surface this could generate a higher load-carrying capacity of the sample during the reciprocating sliding tests. It is well-known that the results of a wear test often depend significantly on the test configuration (i.e., placement of the specimen with respect to the ball counterbody). In the ball-on-disc test (as used in our study), wear debris becomes easily trapped in the wear contact and can promote further wear, whereas in a disc-on-ball or 90° configuration any nonsticking wear debris could fall out of the wear track as a result of the gravitational force. As a result, different test configurations could lead to dissimilar wear behavior in the running-in as well as steady state. This is particularly true in the case of abrasive wear. However, the wear debris detected within the wear track is only of very limited size ($\ll 1$ μm). van der Waals forces dominate at such small sizes, and the material might stick to the sample surface even in disc-on-ball and 90° test configurations. More importantly, the tiny and relatively soft debris is not phase-pure diamond and therefore will not abrade the CVD diamond films. This is also supported by the formation of smooth wear tracks and the absence of any abrasive grooves therein (Figure S1).

We performed a series of micro-Raman measurements across the wear track of the NCD0.2 film after 10 000 sliding cycles to confirm the amorphization of the film surface. The results of these measurements are shown in Figure S4 of the Supporting Information. The data corresponding to the lower B peak (located at ~450 cm^{-1}) are added to Figure S4 to indicate the wear track region. This peak is preferred instead of the diamond peak (at ~1332 cm^{-1}) since the latter position is strongly affected by the high degree of Fano interactions in the heavily B-doped diamond. A drop of the lower B peak intensity is expected due to the decreased thickness of the diamond film at the wear track region, which results in a weaker overall Raman signal compared to the as-grown region. Furthermore, there is a clear increase of the D+G peak intensity (a direct measure of nondiamond, sp^2-rich carbon) in the worn region, with a sharp maximum in the center of the wear track and a less pronounced (local) maximum at the edge of it. These micro-Raman measurements thus evidence an increase of graphitic/amorphous material and debris in and at the edge of the wear track, respectively, through a transition of sp^3-bonded C atoms to sp^2/a-C by the repetitive sliding movement.

3.3.2. Wear Mechanism. Our AFM/TEM analyses show that third-body amorphous material is piled up in-between the grains of the growth surface during sliding (see Figures 4d and 5d). Micro-Raman measurements across the wear track evidenced an increased sp^2/a-C content at the worn surface. Previous experimental studies have also shown that a thin sp^2/a-C layer is formed in the sliding wear contact of polycrystalline diamond films.[60,61] Likewise, the molecular dynamics studies by Pastewka et al.[28] showed the mechanochemical formation of an sp^2/sp-bonded amorphous adlayer during diamond polishing. This is controlled by an atom-by-atom attrition process of nanoscale wear.[62] On the other hand, researchers specified a fracture-based wear mechanism of removal of small film fragments during the initial stage of diamond sliding wear tests.[29,63] Surface asperities of the diamond film interlock with

DOI: 10.1021/acsami.6b08083
ACS Appl. Mater. Interfaces XXXX, XXX, XXX–XXX

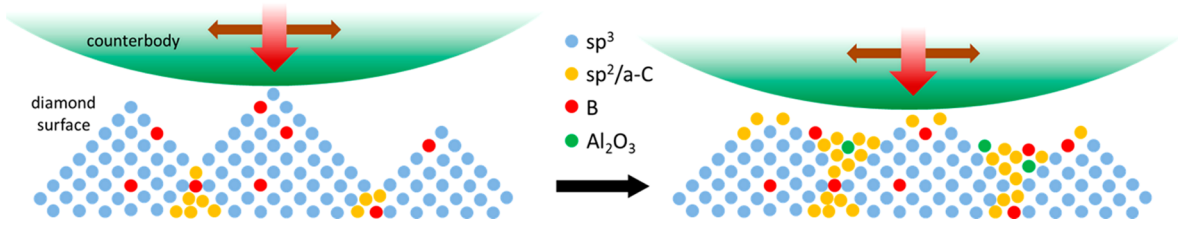

Figure 6. Mechanism of wear on the CVD diamond thin films from an atomistic view. (left) The initial surface state of the diamond film with sharp asperities and the counterbody ball positioned above at the start of the sliding test. (right) Running-in period with its phenomena of asperity removal and debris formation, due to graphitization/amorphization and alumina ball abrasion, which is piled up in-between the grains. The counterbody ball in contact with the B-doped diamond film under sliding conditions leads to the transformation of sp^3-C atoms to sp^2/a-C.

the counterbody surface asperities, resulting in material fracture and abrasion[64] of the diamond film surfaces which leads to a surface planarization. In addition, the asperities experience high contact stresses that assist in the tribochemical reaction[62] and amorphization of the diamond surface.[63,64] The existence of two clearly distinguishable stages of running-in and steady-state sliding in our sliding tests is concluded from the AFM analyses as well as the evolution of the coefficient of friction of all NCD1 films (see Figure S3 of the Supporting Information). The relatively high coefficient of friction during the running-in stage is due to the effectively small contact area (i.e., high local contact pressure) since the counterbody ball slides over a few protruding asperities. This leads to a rapid amorphization of these asperities, which in turn results in a local planarization thereby increasing the contact area. Finally, a constant and low value of the coefficient of friction (and very low rms roughness (Figure S2)) is obtained which corresponds to the steady state. Note that the transition from running-in to steady-state sliding occurs after just around 2000 cycles for all NCD1 films except for the one with the lowest B-doping level (0.6 at. %). This difference indicates the profound effect of B-incorporation on the tribological properties of the diamond films.

Upon B-doping, B−B and B−C clusters are formed within the diamond grains,[65] which exhibit weaker bonding energies compared to the strong hybrid sp^3 C−C bonds,[66] and result in local expansion of the diamond crystal lattice.[67] The incorporated B−B and B−C clusters will thus act as "weak" spots of the lattice, whereby the amorphization is locally enhanced or even initialized during sliding. Figure 6 schematically shows a graphical representation of the atomistic wear behavior. The counterbody and the polycrystalline diamond surface are visible. The latter consists of sp^3-bonded C atoms and B dopants in the grain regions, as well as sp^2/a-C together with B atoms at the grain boundaries. As it can be seen, the sharp sp^3-bonded diamond asperities are flattened due to their partial amorphization during the initial running-in stage, and the amorphous debris is piled up in-between the grains. Both these processes lead to a rapid planarization of the diamond film surface contact. Only a thin layer of sp^2/a-C remains on the contact area of the diamond surface with the counterbody, which will eventually evolve into a thicker (~5 nm) layer as the sliding progresses.[28,60] As the ductility of the remaining sp^2/a-C layer is high, it will eventually lead to the smoothing of the growth surface and even to the formation of nanoscopic ripples.[68] Part of the alumina and sp^2/a-C debris is, however, wiped out of the wear track due to the high lateral forces applied during sliding. In addition, flash asperity heating of the sliding surfaces could lead to local temperatures that strongly exceed the average surface temperature, even under the low-speed sliding conditions applied here.[69] It cannot be ruled out that these higher temperatures further contribute to the amorphization and the a-C debris partially interacting with atmospheric gases, leading to the formation of gaseous species such as CO and CO_2.[28,70]

3.4. Nucleation Surface. Sliding tests were performed on the nucleation surface of the NCD film with the highest B-doping level (2.8 at. %) at 2 N applied normal load. However, as this side of the diamond film is extremely smooth and mirror-like (rms roughness ~0.6 nm), no effective wear was observed with the use of an alumina ball. On the other hand, wear depth data could be extracted when using the three different diamond-coated balls (PN (polished NCD), RN (rough NCD), and RM (rough MCD)) due to the higher reduced elastic modulus and thus higher Hertzian contact pressures associated with the diamond counterbody materials. This reveals that diamond−diamond sliding contacts lead to higher wear of the diamond films than in the case of diamond-alumina sliding contacts. Figure 7 shows the wear depth on the diamond film nucleation side for three different numbers of sliding cycles (i.e., 1000, 3000, and 10 000) and for each type of diamond ball used. Moreover, the wear depth values corresponding to the NCD1 film (growth surface) are also plotted to allow for a direct comparison with the relevant values of the nucleation surface. The wear depth of the nucleation surface is larger when the harder counterbody material is used (i.e., MCD), which explains the shift of the upper curve (RM ball) toward higher wear depth values compared to the other counterbody balls. Specifically, the overall wear depth increases

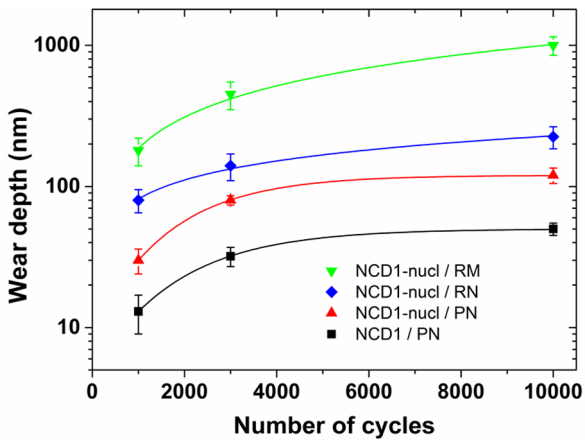

Figure 7. Wear depth vs number of cycles for the NCD1-nucl (2.8 at. % B) and NCD1 (2.8 at. % B) films for sliding against different types of diamond ball counterbodies: polished NCD (PN), rough NCD (RN), and rough MCD (RM) at 2 N normal load.

DOI: 10.1021/acsami.6b08083
ACS Appl. Mater. Interfaces XXXX, XXX, XXX−XXX

by a factor of 2 and 10 when the RM ball is used compared to RN and PN, respectively.

In the case of the PN ball, the wear depth of the nucleation surface is ~2.5× larger than the wear depth on the growth surface of the NCD1 film at all sliding cycles. Specifically, the wear depth of the nucleation and growth surface is 120 and 50 nm after 10 000 cycles, respectively. This difference is attributed to the higher grain boundary line density of the nucleation surface (by 1 order of magnitude) compared to the NCD1 film growth surface, similarly to the comparison of the wear behavior between NCD0.2 and NCD1 films (see Figure 3a). Hence, our study shows that the nucleation surface suffers from a reduced wear resistance compared to the growth surface. This can in turn deteriorate the performance or even become detrimental for applications that require the use of the nucleation surface as the active layer with a highly wear-resistant behavior (such as SSRM tips[12] or MEMS[10,40]).

4. CONCLUSIONS

Our work shows that the wear rate of both NCD and MCD films increases linearly with the B-doping level. In particular, the wear rate increases by a factor of 3 when increasing the B-doping level from 0.6 to 2.8 at. %. The grain size is an additional factor that determines the wear resistance of the diamond films but becomes less prominent for high B-doping levels. The effect of B-doping on the wear behavior of NCD films is supported by nanoindentation measurements which reveal that B-doping strongly deteriorates the mechanical properties such as hardness and elastic modulus, thus resulting in an increased susceptibility to mechanical destabilization. A graphical representation of the wear mechanism of B-doped diamond films is specified based on the experimental observations. This depiction illustrates the flattening of the protruding asperities and a planarization of the film surface during sliding through a mechanochemical amorphization (i.e., a transition of sp^3-bonded C atoms to sp^2/a-C). The enhanced amorphization in diamond films of elevated boron concentrations is attributed to the presence of weaker B−B and B−C bonds, which act as weak points within the diamond lattice and lead to the initiation or enhancement of the amorphization.

Finally, we demonstrate a 2.5× larger wear depth on the nucleation surface compared to the growth surface when sliding against a diamond-coated counterbody (120 and 50 nm after 10 000 sliding cycles, respectively). The higher wear of the nucleation surface is attributed to the higher grain boundary line density, which results in a higher fraction of the soft sp^2/a-C material at the film contact surface. On the contrary, the growth surface contains less grain boundaries, and the diamond grains will first undergo a polishing phase. Our quantitative findings contribute toward a better understanding of the effects of the film morphology and doping level on the wear behavior of B-doped diamond films used for wear-resistant and electrically conductive diamond applications.

■ ASSOCIATED CONTENT

Supporting Information

The Supporting Information is available free of charge on the ACS Publications website at DOI: 10.1021/acsami.6b08083.

Tapping-mode AFM topography images (5 × 5 μm^2 taken from the centers of the wear tracks formed on the NCD1 film (2.8 at. % B-doping level) after sliding for eight different numbers of total cycles at 2 N normal load, rms roughness vs number of cycles for the NCD0.2 (2.8 at. % B-doping level), NCD1 (2.8 at. % B-doping level), and MCD1 (0.6 at. % B-doping level) films at 2 N normal load, coefficient of friction vs number of sliding cycles for the NCD1 films with different B-doping levels, and micro-Raman measurements across the wear track of the NCD0.2 film after 10 000 sliding cycles (PDF)

■ AUTHOR INFORMATION

Corresponding Author

*E-mail: j.g.buijnsters@tudelft.nl. Phone: +31 (0)15 278 5396.

Notes

The authors declare no competing financial interest.

■ ACKNOWLEDGMENTS

The authors acknowledge Diamond Product Solutions for providing the diamond-coated hard metal ball counterbodies and Alain Moussa for his assistance with the AFM measurements of these counterbodies.

■ REFERENCES

(1) May, P. W. The New Diamond Age? *Science* **2008**, *319*, 1490−1491.
(2) Balmer, R. S.; Brandon, J. R.; Clewes, S. L.; Dhillon, H. K.; Dodson, J. M.; Friel, I.; Inglis, P. N.; Madgwick, T. D.; Markham, M. L.; Mollart, T. P.; Perkins, N.; Scarsbrook, G. A.; Twitchen, D. J.; Whitehead, A. J.; Wilman, J. J.; Woollard, S. M. Chemical Vapour Deposition Synthetic Diamond: Materials, Technology and Applications. *J. Phys.: Condens. Matter* **2009**, *21*, 364221.
(3) Artini, C.; Muolo, M. L.; Passerone, A. Diamond-Metal Interfaces in Cutting Tools: a Review. *J. Mater. Sci.* **2012**, *47*, 3252−3264.
(4) Uhlmann, E.; Koenig, J. CVD Diamond Coatings on Geometrically Complex Cutting Tools. *CIRP Ann.* **2009**, *58*, 65−68.
(5) Lux, B.; Haubner, R. Diamond as a Wear-Resistant Coating. *Philos. Trans. R. Soc., A* **1993**, *342*, 297−311.
(6) Buijnsters, J. G.; Shankar, P.; van Enckevort, W. J. P.; Schermer, J. J.; ter Meulen, J. J. Adhesion Analysis of Polycrystalline Diamond Films on Molybdenum by Means of Scratch, Indentation and Sand Abrasion Testing. *Thin Solid Films* **2005**, *474*, 186−196.
(7) Kelly, P. J.; Arnell, R. D.; Hudson, M. D.; Wilson, A. E. J.; Jones, G. Enhanced Mechanical Seal Performance Through CVD Diamond Films. *Vacuum* **2001**, *61*, 61−74.
(8) Gajewski, W.; Achatz, P.; Williams, O. A.; Haenen, K.; Bustarret, E.; Stutzmann, M.; Garrido, J. A. Electronic and Optical Properties of Boron-doped Nanocrystalline Diamond Films. *Phys. Rev. B: Condens. Matter Mater. Phys.* **2009**, *79*, 045206−1−14.
(9) Borst, T. H.; Weis, O. Boron-doped Homoepitaxial Diamond Layers: Fabrication, Characterization, and Electronic Applications. *Phys. Stat. Sol. A* **1996**, *154*, 423−444.
(10) Sumant, A. V.; Auciello, O.; Carpick, R. W.; Srinivasan, S.; Butler, J. E. Ultrananocrystalline and Nanocrystalline Diamond Thin Films for MEMS/NEMS Applications. *MRS Bull.* **2010**, *35*, 281−288.
(11) Sepulveda, N.; Aslam, D.; Sullivan, J. P. Polycrystalline Diamond MEMS Resonator Technology for Sensor Applications. *Diamond Relat. Mater.* **2006**, *15*, 398−403.
(12) Hantschel, T.; Niedermann, P.; Trenkler, T.; Vandervorst, W. Highly Conductive Diamond Probes for Scanning Spreading Resistance Microscopy. *Appl. Phys. Lett.* **2000**, *76*, 1603−1605.
(13) De Wolf, P.; Snauwaert, J.; Hellemans, L.; Clarysse, T.; Vandervorst, W.; D'Olieslaeger, M.; Quaeyhaegens, D. Lateral and Vertical Dopant Profiling in Semiconductors by Atomic Force Microscopy Using Conducting Tips. *J. Vac. Sci. Technol., A* **1995**, *13*, 1699−1704.
(14) Smirnov, W.; Kriele, A.; Hoffmann, R.; Sillero, E.; Hees, J.; Williams, O. A.; Yang, N. J.; Kranz, C.; Nebel, C. E. Diamond-Modified AFM Probes: From Diamond Nanowires to Atomic Force

DOI: 10.1021/acsami.6b08083
ACS Appl. Mater. Interfaces XXXX, XXX, XXX−XXX

Microscopy-Integrated Boron-doped Diamond Electrodes. *Anal. Chem.* **2011**, *83*, 4936−4941.
(15) Zanin, H.; May, P. W.; Fermin, D. J.; Plana, D.; Vieira, S. M. C.; Milne, W. I.; Corat, E. J. Porous Boron-doped Diamond/Carbon Nanotube Electrodes. *ACS Appl. Mater. Interfaces* **2014**, *6*, 990−995.
(16) Kraft, A. Doped Diamond: A Compact Review on a New, Versatile Electrode Material. *Int. J. Electrochem. Sci.* **2007**, *2*, 355−385.
(17) Zeng, H.; Konicek, A. R.; Moldovan, N.; Mangolini, F.; Jacobs, T.; Wylie, I.; Arumugam, P. U.; Siddiqui, S.; Carpick, R. W.; Carlisle, J. A. Boron-doped Ultrananocrystalline Diamond Synthesized With an H-Rich/Ar-Lean Gas System. *Carbon* **2015**, *84*, 103−117.
(18) Ochiai, T.; Nakata, K.; Murakami, T.; Fujishima, A.; Yao, Y. Y.; Tryk, D. A.; Kubota, Y. Development of Solar-Driven Electrochemical and Photocatalytic Water Treatment System Using a Boron-doped Diamond Electrode and TiO_2 Photocatalyst. *Water Res.* **2010**, *44*, 904−910.
(19) Ayata, S.; Stefanova, A.; Ernst, S.; Baltruschat, H. The Electro-oxidation of Water and Alcohols at BDD in Hexafluoroisopropanol. *J. Electroanal. Chem.* **2013**, *701*, 1−6.
(20) Muna, G. W.; Tasheva, N.; Swian, G. M. Electro-oxidation and Amperometric Detection of Chlorinated Phenols at Boron-doped Diamond Electrodes: A Comparison of Microcrystalline and Nano-crystalline Thin Films. *Environ. Sci. Technol.* **2004**, *38*, 3674−3682.
(21) Gao, F.; Nebel, C. E. Diamond-Based Supercapacitors: Realization and Properties. *ACS Appl. Mater. Interfaces* **2015**, DOI: 10.1021/acsami.5b07027.
(22) Chan, H.-Y.; Aslam, D. M.; Wiler, J. A.; Casey, B. A Novel Diamond Microprobe for Neuro-chemical and -electrical Recording in Neural Prosthesis. *J. Microelectromech. Syst.* **2009**, *18*, 511−521.
(23) Caterino, R.; Csiki, R.; Wiesinger, M.; Sachsenhauser, M.; Stutzmann, M.; Garrido, J. A.; Cattani-Scholz, A.; Speranza, G.; Janssens, S. D.; Haenen, K. Organophosphonate Biofunctionalization of Diamond Electrodes. *ACS Appl. Mater. Interfaces* **2014**, *6*, 13909−13916.
(24) Tolkowsky, W. Research on the Abrading, Grinding or Polishing of Diamond. *D.Sc. Thesis*, City and Guilds College, University of London: UK, 1920.
(25) Thomas, E. L. H.; Mandal, S.; Brousseau, E. B.; Williams, O. A. Silica Based Polishing of {100} and {111} Single Crystal Diamond. *Sci. Technol. Adv. Mater.* **2014**, *15*, 035013.
(26) Derry, T. E.; van der Berg, N.; Makau, N. W. Diamond Surfaces Polished Both Mechanically and Manually; an Atomic Force Microscopy (AFM) Study. *Diamond Relat. Mater.* **2008**, *17*, 127−136.
(27) Hird, J. R.; Field, J. E. A Wear Mechanism Map for the Diamond Polishing Process. *Wear* **2005**, *258*, 18−25.
(28) Pastewka, L.; Moser, S.; Gumbsch, P.; Moseler, M. Anisotropic Mechanical Amorphization Drives Wear in Diamond. *Nat. Mater.* **2011**, *10*, 34−38.
(29) Mohrbacher, H.; Blanpain, B.; Celis, J. P.; Roos, J. R. Low Amplitude Oscillating Sliding Wear on Chemically Vapour Deposited Diamond Coatings. *Diamond Relat. Mater.* **1993**, *2*, 879−884.
(30) Perry, S. S.; Ager, J. W., III; Somorjai, G. A. Combined Surface Characterization and Tribological (Friction and Wear) Studies of CVD Diamond Films. *J. Mater. Res.* **1993**, *8*, 2577−2586.
(31) Liu, E.; Blanpain, B.; Celis, J. P. Fretting Friction and Wear of Polycrystalline Diamond Coatings. *Diamond Relat. Mater.* **1996**, *5*, 649−653.
(32) Erdemir, A.; Halter, M.; Fenske, G. R.; Zuiker, C.; Csencsits, R.; Krauss, A. R.; Gruen, D. M. Friction and Wear Mechanisms of Smooth Diamond Films During Sliding in Air and Dry Nitrogen. *Tribol. Trans.* **1997**, *40*, 667−675.
(33) Sankaran, K. J.; Kumar, N.; Kurian, J.; Ramadoss, R.; Chen, H. C.; Dash, S.; Tyagi, A. K.; Lee, C. Y.; Tai, N. H.; Lin, I.-N. Improvement in Tribological Properties by Modification of Grain Boundary and Microstructure of Ultrananocrystalline Diamond Films. *ACS Appl. Mater. Interfaces* **2013**, *5*, 3614−3624.
(34) Lei, X.; Shen, B.; Chen, S.; Wang, L.; Sun, F. Tribological Behavior Between Micro- and Nano-crystalline Diamond Films Under Dry Sliding and Water Lubrication. *Tribol. Int.* **2014**, *69*, 118−127.
(35) Liang, Q.; Stanishevsky, A.; Vohra, Y. K. Tribological Properties of Undoped and Boron-doped Nanocrystalline Diamond Films. *Thin Solid Films* **2008**, *517*, 800−804.
(36) Wang, L.; Lei, X.; Shen, B.; Sun, F.; Zhang, Z. Tribological Properties and Cutting Performance of Boron and Silicon Doped Diamond Films on Co-cemented Tungsten Carbide Inserts. *Diamond Relat. Mater.* **2013**, *33*, 54−62.
(37) Ralchenko, V.; Saveliev, A.; Voronina, S.; Dementjev, A.; Maslakov, K.; Salerno, M.; Podesta, A.; Milani, P. In *Synthesis, Properties and Applications of Ultrananocrystalline Diamond*; Gruen, D. M., Shenderova, O. A., Vul', A. Y., Eds.; Springer: St. Petersburg, 2005; Chapter 9, pp 109−124.
(38) Tsigkourakos, M.; Hantschel, T.; Simon, D. K.; Nuytten, T.; Verhulst, A. S.; Douhard, B.; Vandervorst, W. On the Local Conductivity of Individual Diamond Seeds and Their Impact on the Interfacial Resistance of Boron-doped Diamond Films. *Carbon* **2014**, *79*, 103−112.
(39) Tsigkourakos, M.; Hantschel, T.; Xu, Z.; Douhard, B.; Meersschaut, J.; Zou, Y.; Larsson, K.; Boman, M.; Vandervorst, W. Suppression of Boron Incorporation at the Early Growth Phases of Boron-doped Diamond Thin Films. *Phys. Status Solidi A* **2015**, *212*, 2595−2599.
(40) Sumant, A. V.; Grierson, D. S.; Gerbi, J. E.; Birrell, J.; Lanke, U. D.; Auciello, O.; Carlisle, J. A.; Carpick, R. W. Toward the Ultimate Tribological Interface: Surface Chemistry and Nanotribology of Ultrananocrystalline Diamond. *Adv. Mater.* **2005**, *17*, 1039−1045.
(41) Sumant, A. V.; Grierson, D. S.; Gerbi, J. E.; Carlisle, J. A.; Auciello, O.; Carpick, R. W. Surface Chemistry and Bonding Configuration of Ultrananocrystalline Diamond Surfaces and their Effects on Nanotribological Properties. *Phys. Rev. B: Condens. Matter Mater. Phys.* **2007**, *76*, 235429.
(42) Williams, O. A.; Nesladek, M.; Daenen, M.; Michaelson, S.; Hoffman, A.; Osawa, E.; Haenen, K.; Jackman, R. B. Growth, Electronic Properties and Applications of Nanodiamond. *Diamond Relat. Mater.* **2008**, *17*, 1080−1088.
(43) Tsigkourakos, M.; Hantschel, T.; Janssens, S. D.; Haenen, K.; Vandervorst, W. Spin-seeding Approach for Diamond Growth on Large Area Silicon-wafer Substrates. *Phys. Status Solidi A* **2012**, *209*, 1659−1663.
(44) Zimmer, J.; Hantschel, T.; Chandler, G.; Vandervorst, W.; Peralta, M. Boron Doping in Hot Filament MCD and NCD Diamond Films. *MRS Online Proc. Libr.* **2009**, *1203*, 1203-J12−01.
(45) Mohrbacher, H.; Celis, J. P.; Roos, J. R. Laboratory Testing of Displacement and Load Induced Fretting. *Tribol. Int.* **1995**, *28*, 269−278.
(46) Oliver, W. C.; Pharr, G. M. An Improved Technique for Determining Hardness and Elastic Modulus Using Load and Displacement Sensing Indentation Experiments. *J. Mater. Res.* **1992**, *7*, 1564−1583.
(47) Archard, J. F. Contact and Rubbing of Flat Surfaces. *J. Appl. Phys.* **1953**, *24*, 981−988.
(48) Bernard, M.; Deneuville, A.; Muret, P. Non-destructive Determination of the Boron Concentration of Heavily Doped Metallic Diamond Thin Films from Raman Spectroscopy. *Diamond Relat. Mater.* **2004**, *13*, 282−286.
(49) Ager, J. W., III; Walukiewicz, W.; McCluskey, M.; Plano, M. A.; Landstrass, M. I. Fano Interference of the Raman Phonon in Heavily Boron-doped Diamond Films Grown by Chemical Vapor Deposition. *Appl. Phys. Lett.* **1995**, *66*, 616−618.
(50) Ushizawa, K.; Watanabe, K.; Ando, T.; Sakaguchi, I.; Nishitani-Gamo, M.; Sato, Y.; Kanda, H. Boron Concentration Dependence of Raman Spectra on {100} and {111} Facets of B-doped CVD Diamond. *Diamond Relat. Mater.* **1998**, *7*, 1719−1722.
(51) Ferrari, A. C.; Robertson, J. Resonant Raman Spectroscopy of Disordered, Amorphous, and Diamondlike Carbon. *Phys. Rev. B: Condens. Matter Mater. Phys.* **2001**, *64*, 075414.
(52) Buijnsters, J. G.; Celis, J.-P.; Hendrikx, R. W. A.; Vázquez, L. Metallic Seed Nanolayers for Enhanced Nucleation of Nanocrystalline Diamond Thin Films. *J. Phys. Chem. C* **2013**, *117*, 23322−23332.

DOI: 10.1021/acsami.6b08083
ACS Appl. Mater. Interfaces XXXX, XXX, XXX−XXX

(53) Bundy, F. P.; Hall, H. T.; Strong, H. M.; Wentorf, R. H. Man-Made Diamonds. *Nature* **1955**, *176*, 51−55.
(54) Brookes, C. A.; Brookes, E. J. Diamond in Perspective: a Review of Mechanical Properties of Natural Diamond. *Diamond Relat. Mater.* **1991**, *1*, 13−17.
(55) Irifune, T.; Kurio, A.; Sakamoto, S.; Inoue, T.; Sumiya, H. Materials: Ultrahard Polycrystalline Diamond from Graphite. *Nature* **2003**, *421*, 599−600.
(56) Nitti, M. A.; Cicala, G.; Brescia, R.; Romeo, A.; Guion, J. B.; Perna, G.; Capozzi, V. Mechanical Properties of MWPECVD Diamond Coatings on Si Substrate via Nanoindentation. *Diamond Relat. Mater.* **2011**, *20*, 221−226.
(57) Roy, M.; Ghodbane, S.; Koch, T.; Pauschitz, A.; Steinmller-Nethl, D.; Tomala, A.; Tomastik, C.; Franek, F. Tribological Investigation of Nanocrystalline Diamond Films at Low Load Under Different Tribosystems. *Diamond Relat. Mater.* **2011**, *20*, 573−583.
(58) Li, M. M.; Fan, X.; Zheng, W. T. First-Principle Calculations on The Structural Stability and Electronic Properties of Superhard B_xC_y Compounds. *J. Phys.: Condens. Matter* **2013**, *25*, 425502.
(59) Zarechnaya, E. Yu.; Isaev, E. I.; Simak, S. I.; Vekilov, Yu.; Kh; Dubrovinsky, L. S.; Dubrovinskaia, N. A.; Abrikosov, I. A. Ground-State Properties of Boron-Doped Diamond. *J. Exp. Theor. Phys.* **2008**, *106* (4), 781−787.
(60) Konicek, A. R.; Grierson, D. S.; Gilbert, P. U. P. A.; Sawyer, W. G.; Sumant, A. V.; Carpick, R. W. Origin of Ultralow Friction and Wear in Ultrananocrystalline Diamond. *Phys. Rev. Lett.* **2008**, *100*, 235502−1.
(61) Zhang, X.; Schneider, R.; Muller, E.; Mee, M.; Meier, S.; Gumbsch, P.; Gerthsen, D. Electron Microscopic Evidence for a Tribologically Induced Phase Transformation as the Origin of Wear in Diamond. *J. Appl. Phys.* **2014**, *115*, 063508.
(62) Jacobs, T. D. B.; Carpick, R. W. Nanoscale Wear as a Stress-assisted Chemical Reaction. *Nat. Nanotechnol.* **2013**, *8*, 108−112.
(63) Chromik, R. R.; Winfrey, A. L.; Luning, J.; Nemanich, R. J.; Wahl, K. J. Run-in Behavior of Nanocrystalline Diamond Coatings Studied by In Situ Tribometry. *Wear* **2008**, *265*, 477−489.
(64) Holmberg, K.; Ronkainen, H.; Laukkanen, A.; Wallin, K. Friction and Wear of Coated Surfaces-Scales, Modelling and Simulation of Tribomechanisms. *Surf. Coat. Technol.* **2007**, *202*, 1034−1049.
(65) Ashcheulov, P.; Sebera, J.; Kovalenko, A.; Petrak, V.; Fendrych, F.; Nesladek, M.; Taylor, A.; Vlckova Zivcova, Z.; Frank, O.; Kavan, L.; Dracinsky, M.; Hubik, P.; Vacik, J.; Kraus, I.; Kratochvılova, I. Conductivity of Boron-doped Polycrystalline Diamond Films: Influence of Specific Boron Defects. *Eur. Phys. J. B* **2013**, *86*, 443−451.
(66) Brenner, D. W.; Shenderova, O. A. Theory and Modelling of Diamond Fracture from an Atomic Perspective. *Philos. Trans. R. Soc., A* **2015**, *373*, 20140139.
(67) Zhao, S.; Larsson, K. Theoretical Study of the Energetic Stability and Geometry of Terminated and B-doped Diamond (111) Surfaces. *J. Phys. Chem. C* **2014**, *118*, 1944−1957.
(68) Podgursky, V.; Hantschel, T.; Bogatov, A.; Kimmari, E.; Antonov, M.; Viljus, M.; Mikli, V.; Tsigkourakos, M.; Vandervorst, W.; Buijnsters, J. G.; Raadik, A. T.; Kulu, P. Rippling on Wear Scar Surfaces of Nanocrystalline Diamond Films After Reciprocating Sliding Against Ceramic Balls. *Tribol. Lett.* **2014**, *55*, 493−501.
(69) Kalin, M. Influence of Flash Temperatures on the Tribological Behaviour in Low-speed Sliding: A Review. *Mater. Sci. Eng., A* **2004**, *374*, 390−397.
(70) Kunze, T.; Posselt, M.; Gemming, S.; Seifert, G.; Konicek, A. R.; Carpick, R. W.; Pastewka, L.; Moseler, M. Wear, Plasticity, and Rehybridization in Tetrahedral Amorphous Carbon. *Tribol. Lett.* **2014**, *53*, 119−126.

DOI: 10.1021/acsami.6b08083
ACS Appl. Mater. Interfaces XXXX, XXX, XXX−XXX